Sim, W. W. *et al.* (2012). *Géotechnique* **62**, No. 12, 1067–1079 [http://dx.doi.org/10.1680/geot.10.P.142]

One-***g*** shaking-table experiments on buried pipelines crossing a strike-slip fault

W. W. SIM*, I. TOWHATA† and S. YAMADA†

Buried pipelines provide essential services to the urban population, and as a result of their geographical dispersion they remain particularly vulnerable to damage caused by natural disasters. Among many damage mechanisms, the present study addresses those induced by seismic fault action and its related ground distortion. A better understanding of the factors influencing the forces acting on buried pipelines due to imposed ground displacements will permit more appropriate design of pipelines in the future, and contribute towards reducing damage incurred by the buried pipes. To this end, 1*g* shaking-table experiments were performed on buried model pipelines installed in Toyoura sand, which were instrumented to monitor strain. The system was subjected to four different levels of dynamic excitation and right-lateral strike-slip faulting. The experiments indicate that simultaneous shaking and faulting, which is a more realistic condition than tests performed without shaking, reduce the measured pipe strains. Tests also indicated that there is a linear decrease in the maximum strains experienced by the buried pipe as the sine of the pipe-fault crossing angle decreases, and that there is a non-linear relationship between the relative density and the strains experienced by the buried pipe.

KEYWORDS: buried structures; deformation; earthquakes; model tests; soil/structure interaction

Les canalisations souterraines assurent la distribution des fournitures essentielles dans les populations urbaines ; en conséquence de leur dispersion géographique, elles restent particulièrement vulnérables aux dommages causés par des désastres naturels. Parmi les nombreux mécanismes d'endommagement, la présente étude se penche ceux qui sont induits par les actions de fautes séismiques et les déformations du sol qui en découlent. Une meilleure connaissance des facteurs influant sur les forces qui agissent sur les canalisations souterraines en raison de déplacements du sol imposé permettrait de concevoir, dans l'avenir, des types de canalisations mieux appropriées, en contribuant à une réduction des dommages subis par les canalisations souterraines. A cette fin, on a procédé à des expériences avec table secouant à 1 *g* sur des maquettes de canalisations souterraines, installées dans du sable de Toyoura, et instrumentées pour contrôler les contraintes. On a soumis le système à quatre niveaux d'excitation dynamique et des déformations par décrochement droite/latérales. Les expériences indiquent que les secousses et failles simultanées, plus réalistes que les essais effectués sans secousses, réduisent les contraintes mesurées sur les canalisations ; elles indiquent également qu'une augmentation linéaire des contraintes maximales subies par la canalisation souterraine comme sinus de l'angle de croisement canalisation /faille diminue, et que l'on relève une relation non linéaire entre la densité relative et les contraintes subies par la canalisation souterraine.

INTRODUCTION

Pipe networks often cover a wide area, and may need to cross active faults. Fig. 1 illustrates seismic damage to buried pipelines. Damage to a water pipeline crossing a causative fault of the 1990 Manjil earthquake in Iran is shown in Figs 1(a) and 1(b), and damage to pipelines due to collapse of a highway embankment during the 2004 Niigata-ken Chuetsu earthquake in Japan is shown in Fig. 1(c). Motivated by such events, this study focuses primarily on small-diameter (~60 mm) local gas pipelines, typically installed within 1·5 m from the ground surface. These local gas pipelines convey vital energy services that form extensive subterranean networks throughout many modern cities.

Earthquake engineers have not studied soil response due to fault rupture extensively, but some meaningful contributions have been made by Newmark & Hall (1975), Taniyama & Watanabe (1998); Ueta & Tani (1999), Bray (2001), Koyama & Tani (2003), and Konagai (2005). Studies that have specifically considered the seismic behaviour of embedded pipes undergoing fault rupture and the development of design methodology include contributions by Desmond *et al.* (1995), Kennedy *et al.* (1977), Wang & Yeh (1985), Wang & Wang (1995), Takada *et al.* (2001), Yasuda & Hori (2006), Yasuda *et al.* (2007), and Abdoun *et al.* (2009).

Serious concern has been raised in recent years about the seismic safety of many structures subjected to the strong levels of acceleration that were recorded in a number of earthquakes in the 1990s, such as accelerations of 1·8***g*** recorded in the 1994 Northridge earthquake. As previous model studies on pipelines crossing active faults have largely been performed without simultaneous dynamic excitation (Trautmann & O'Rourke, 1985; Ha *et al.*, 2008, O'Rourke *et al.*, 2008), concerns have been raised over the possible underprediction of soil loads on the pipe, should the dynamic component of soil loading be superimposed on the established static case. The experiments described here aimed to reproduce the loading conditions on embedded pipelines subjected to earthquake-induced shear failure of the surrounding ground. Recent experience of seismic damage demonstrates that buried pipelines are also vulnerable to embankment collapse, as depicted by Fig. 1(c), and documented by Rathje *et al.* (2006). Considering the effects of fault action and embankment failure on embedded pipes to be the same, in the sense of shear failure of the soil, this study makes a contribution to understanding both damage

Manuscript received 27 December 2010; revised manuscript accepted 21 March 2012. Published online ahead of print 22 August 2012. Discussion on this paper closes on 1 May 2013, for further details see p. ii.

* Geotechnics Section, Department of Civil and Environmental Engineering, Imperial College, London, UK.
† Department of Civil Engineering, University of Tokyo, Tokyo, Japan.

Fig. 1. Fault-induced damage of embedded pipeline during 1990 Manjil earthquake, Iran: (a) view of damage from a distance; (b) close-up of pipeline failure. (c) Damage to buried pipes embedded in an embankment along Highway 17, Kawaguchi, during 2004 Niigata-ken Chuetsu earthquake, Japan (37·291°N, 138·836°E)

due to a fault rupture and damage due to interception of the pipe by a slip plane during earthquake-triggered slope failure.

EXPERIMENTAL SET-UP

Apparatus

A new apparatus (Fig. 2) was designed and built to simulate a strike-slip fault. The apparatus was designed to be connected to the shaking table to allow simultaneous faulting and dynamic horizontal excitation. The strike-slip apparatus consists of a reaction frame and a split box, half of which is stationary and half of which rests on rails, allowing it to be moved horizontally past the stationary block, and thus reproducing a strike-slip fault. The split-box tank, which is 90 cm by 90 cm wide and 60 cm deep, is shown schematically in Fig. 2. The strike-slip fault movement is powered by a gas cylinder that applies a constant force of 5 kPa to the moving block. The gas cylinder produced model fault rupture speeds ranging from 0·425 to 0·882 cm/s, with an average of 0·599 cm/s. The model fault rupture is essentially static, with the near-field ground velocity of real ground being sufficiently slow to be considered as such (Kennedy *et al.*, 1977), and was kept constant to eliminate it as a variable from these experiments.

Instrumentation

Accelerations were monitored at the base of both the stationary and moving blocks by accelerometers AC68 and AC72, and for Tests 08 to 49 inclusive horizontal displacement of the fault was monitored through laser displacement sensors placed on the outside flange of the stationary block (Fig. 2). As pipe dimensions can vary from site to site in the field, experiments were performed on a range of pipe flexural rigidities. Two different materials with two different diameters were chosen for the model pipes, so that four flexural rigidities were examined (Table 1).

A plan view of all four instrumented pipes used in this study is shown in Fig. 3. The reference test, with which variations in maximum acceleration, pipe-fault crossing angle, soil density and pipe rigidity were compared, used the 2 cm diameter acrylic (AR20) pipe. Each model pipe was designed to be 86 cm long, to allow space for installation within the split box. All the model pipes were instrumented with waterproofed strain gauges at 5 cm intervals along the spring lines, with a 3 cm offset from each end, as shown inset in Fig. 3. The line of strain gauges in the α line face side C of the strike-slip box, while those in the β line of strain gauges face side A, as shown in Fig. 2. It was decided not to fix either end of the pipe to the apparatus, as this would have resulted in strains being developed in the pipe during faulting, irrespective of the presence of any soil. Thus both ends of the model pipeline were designed to be free, and displacements were monitored by draw-wire displacement sensors. These sensors were attached to the pipe by screw-heads on the apex of the pipe (Fig. 3, inset).

Test method

The experiments were designed to examine the effect of four main factors: the pipe-fault crossing angle, θ; the acceleration intensity, A_{max}; the soil stiffness in terms of density, D_r; and the pipe stiffness, EI, as the magnitude of fault displacement, δ, increased. The experiments focus on pipes that are buried at a shallow depth, above the water table: therefore the surrounding soil was considered to be dry. All tests were performed with an instrumented pipe embedded in air-pluviated dry Toyoura sand, 10 cm above the strike-slip fault with 10 cm of overburden (Fig. 2(b)). Each pipe was installed with the strain gauges oriented to measure the dominant strains developed in the horizontal plane, except for Test 01, in which the pipe was installed to capture the strains developed in the vertical plane.

The 1g conditions of the experiments required the density of the model soil to be lower than that of the prototype, to account for the heightened dilatancy of sand when subjected to reduced overburden stress conditions (Towhata, 2008). In situ, the overburden stresses are typically up to 10 times greater than those reproduced in the experimental model: consequently, a relative density (D_r) of 60% in the model tests was employed at model scale to represent an in situ relative density of 70–80%.

In total, seven different pipe-fault crossing angles, four different levels of acceleration and three different relative densities of the backfill soil were examined through 39 separate experiments. The reference test was considered to be an AR20 pipe crossing at 90° to the fault, with a backfill of dry Toyoura sand placed at a relative density of 60% under no shaking (Test 05). The tests are divided into four

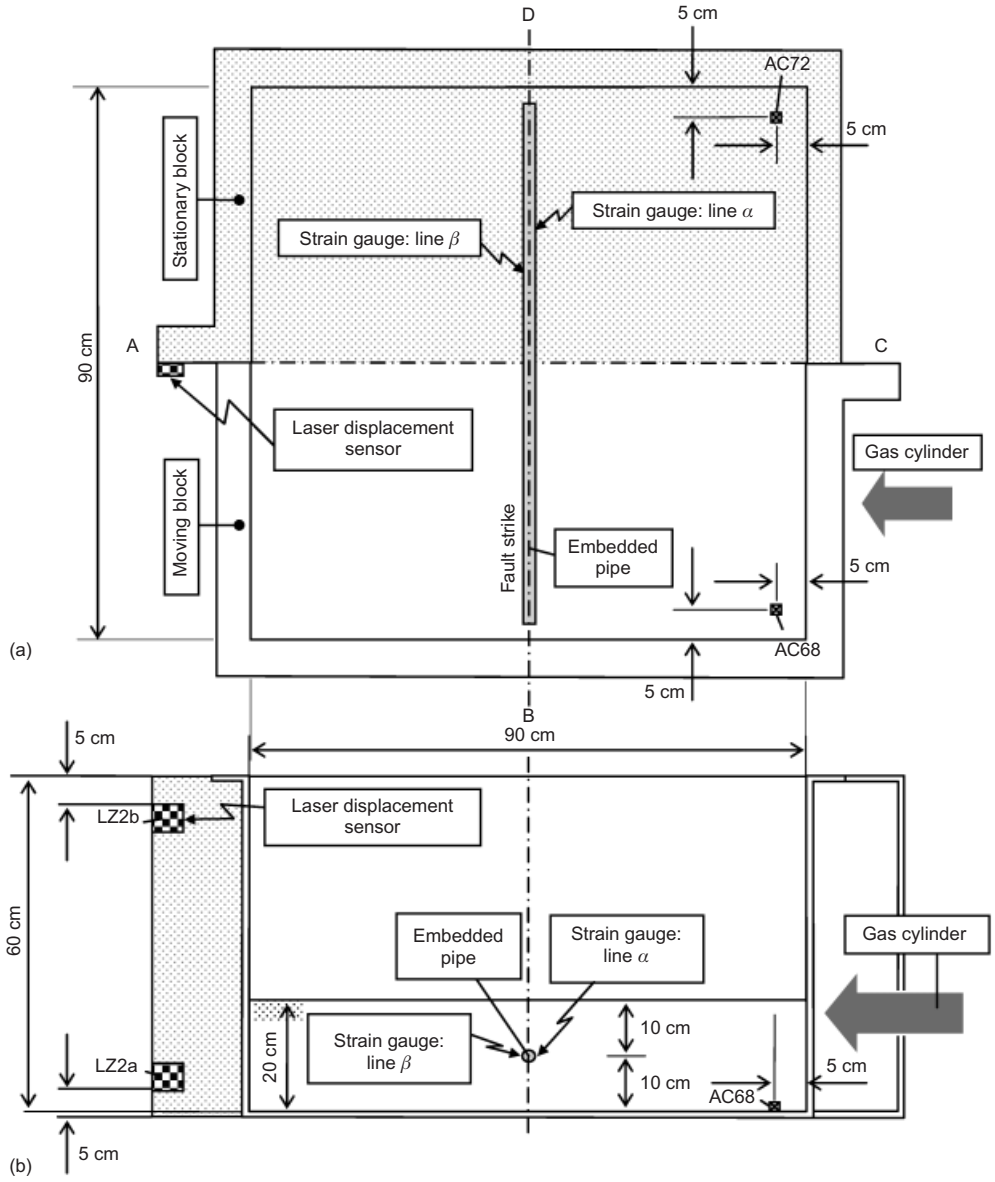

Fig. 2. Schematic diagram of split-box apparatus: (a) plan view; (b) cross-section A–C

Table 1. Model pipe properties

Property	Pipe label			
	AR20	AR40	PE20	PE40
Material	Acrylic		Soft polyethylene	
Outer diameter, d_{out}: mm	20	40	22	42
Internal diameter, d_{int}: mm	12	36	16	35
Wall thickness, t: mm	4·0	2·0	3·0	3·5
Elastic modulus, E: MPa	3200	3200	235	235
Second moment of inertia, I: mm^4	$6{\cdot}84 \times 10^3$	$43{\cdot}22 \times 10^3$	$6{\cdot}33 \times 10^3$	$79{\cdot}08 \times 10^3$
Flexural rigidity, EI: Pa m^4	218·75	1382·90	14·87	185·85
Flexural rigidity (relative to AR20)	EI	$6{\cdot}32EI$	$0{\cdot}07EI$	$0{\cdot}85EI$
Normalisation factor $\left(\frac{E_{pipe}}{E_{AR20}} \times \frac{I_{pipe}}{I_{AR20}}\right)^{0{\cdot}25}$	1·00	1·59	0·27	0·50

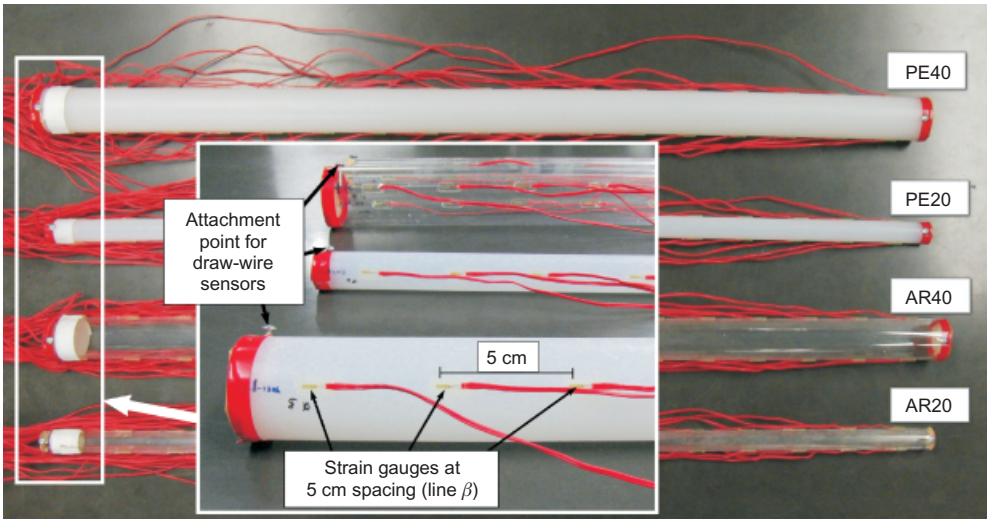

Fig. 3. Plan view of instrumented pipes used in experiments: PE40, 42 mm diameter polyethylene pipe; PE20, 22 mm diameter polyethylene pipe; AR40, 40 mm diameter acrylic pipe; AR20, 20 mm diameter acrylic pipe. Inset: detail of pasted gauges and screw-head point used to attach draw-wire displacement sensors

groups (Z, A, B and C). Test group Z encompasses two tests, and examines the magnitude of strains developed in the vertical plane in comparison with those developed in the horizontal plane, in order to verify the validity of monitoring only the horizontal strains for the rest of this study. Test group A consists of 28 experiments examining the effect of pipe-fault crossing angle and level of acceleration on the 20 mm diameter AR20 pipes buried in dry Toyoura sand placed at $D_r = 60\%$. In test group A, seven different pipe-fault crossing angles were examined at four different levels of acceleration (A_{max}). In addition to the pipe being installed perpendicular to the strike-slip fault ($\theta = 90°$) pipe-fault crossing angles of 60°, 45° and 30° inducing axial tension and compression, as indicated in Fig. 4, were examined. Within test group A the different levels of maximum acceleration (A_{max}) examined were 0·0***g***, 0·2***g***, 0·5***g*** and 0·8***g***. Test group B, which consisted of six experiments, addressed the effect of soil density on a 20 mm AR20 pipe crossing at 90° to the strike-slip fault by comparing tests performed at three different relative densities ($D_r = 40\%$, 60% and 80%), without shaking and with $A_{max} = 0{\cdot}5\boldsymbol{g}$, allowing a correlation to be drawn between the relative density of backfill sand and pipe response. Test group C consisted of eight experiments, and studied the effect of pipe rigidity on pipe response both without shaking and with $A_{max} = 0{\cdot}5\boldsymbol{g}$. Group C tests were performed in dry Toyoura sand placed at $D_r = 60\%$, with different pipes (shown in Fig. 3) embedded perpendicular to the fault, again considering the no-shaking case and the $A_{max} = 0{\cdot}5\boldsymbol{g}$ case.

The applied acceleration was sinusoidal, unidirectional, constant in frequency, and programmed to increase the applied acceleration gradually from zero to the prescribed maximum level, A_{max}, over a 2 s interval. A_{max} was maintained for 16 s, after which the acceleration was gradually reduced back to zero over a further 2 s, as shown schematically in Fig. 5. The laws of similitude proposed by Iai (1989) are not entirely applicable to this 1***g*** loading scenario, due to the large deformations imposed on the soil through the simulated faulting. Therefore a frequency of 10 Hz was chosen to represent an earthquake with ground displacement larger than that of the average grain size of the soil. It is acknowledged that the nature of the chosen acceleration regime means that wave passage effects and incoherence cannot be accounted for in this study.

TEST RESULTS

Fault displacement, δ

Figures 6(a) and 6(b) give respectively the variation in strain and fault displacement with time for a representative test where shaking is applied during faulting. The measured pipe strains were observed to be directly affected by the

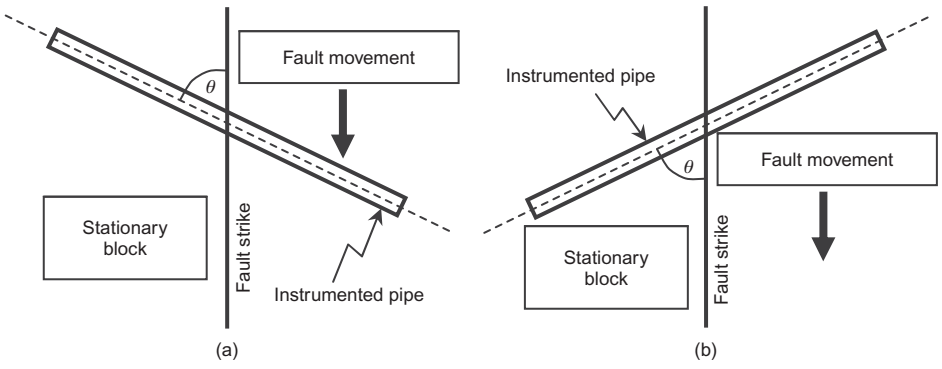

Fig. 4. Plan view of pipe crossing strike-slip fault at angle *θ*, causing: (a) tension; (b) compression in the pipe

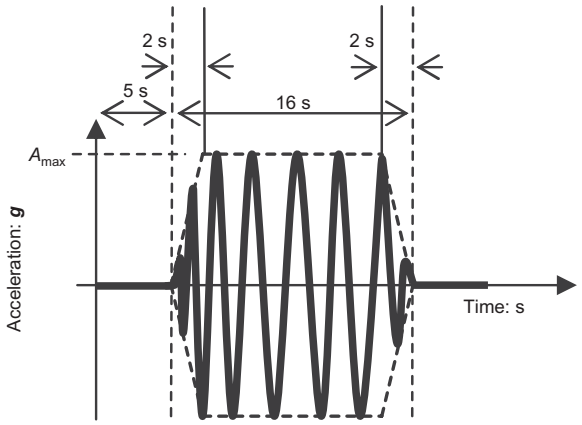

Fig. 5. Schematic diagram of applied base acceleration

magnitude of δ, as indicated in Fig. 6. The mean trend is for the strain in Fig. 6(a) to increase with δ (Fig. 6(b)), indicating the significance of fault action on the distortion of an embedded pipe. In contrast, the cyclic component of strain (represented by the 'original' strain recording in Fig. 6(a)), produced by the inertial effect of 0·5***g*** strong ground shaking, is much smaller (Fig. 6(a)). After 17·5 s, when the fault motion has ceased, the mean strain decreases to some extent. Although the exact reason for this is still unknown, it is possibly related to the rate-dependent nature of creep distortion of sand.

As the first seven tests (Test 01 to 07) were performed prior to the installation of the two laser displacement sensors, the time and magnitude of δ were obtained from video footage of the split box during faulting. In Test 44 the data loggers failed to record any laser displacement or draw-wire displacement data. Therefore the times at which the 1 cm increments of δ occurred were inferred from the time lapse between each centimetre of displacement observed in the other tests performed under the same level of acceleration. In all cases, the maximum value of δ exceeded 5 cm, with the exception of Test 02, which was stopped at $\delta = 4{\cdot}5$ cm.

Data processing

Data obtained from the data loggers were filtered to remove the dynamic component and noise of the recorded strains using adjacent averaging smoothing, leaving the static component, represented by the 'smoothed' strain in Fig. 6(a). As a result of the harsh experimental conditions that the instrumented pipe was exposed to, combined with the delicate nature of the strain gauges, several of the gauges failed during testing. For these cases the data were omitted from the dataset. The distance from the fault was measured along the major axis of the pipe relative to the fault strike, with positive distance from the fault representing a point positioned over the moving block, and negative distance from the fault overlying the stationary block.

The smoothed data can be used to calculate the bending strain (equation (1)) or axial strain (equation (2)) at positions along the major axis of the pipe, where a pair of strain gauges is pasted, by comparing the strain gauge reading along line α, ε_α, with the readings along line β, ε_β. As the strain gauges were set to measure tension in the pipe to be positive, and compression as negative strain values, the strain reading along line β is opposite in sign to that along line α. The bending strain (ε_b) and axial strain (ε_a) were then taken as

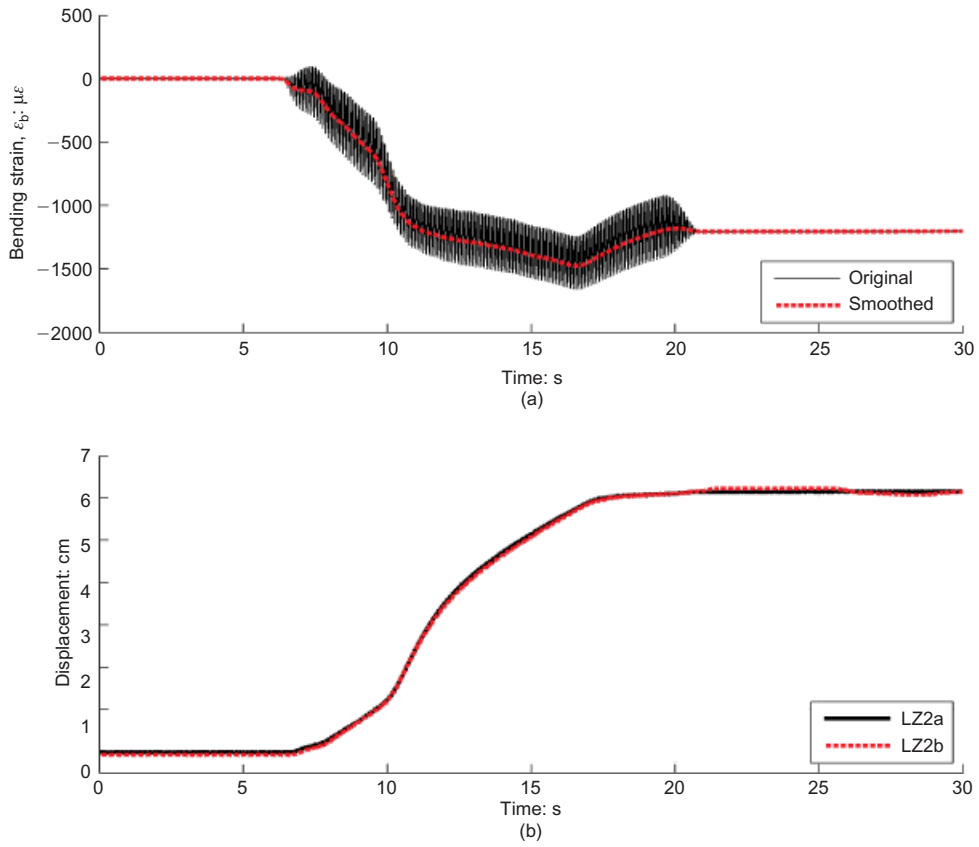

Fig. 6. Time history plots for Test 12: (a) recorded and smoothed strain gauge readings in line β, 15 cm from fault on moving block; (b) laser displacement transducers LZ2a and LZ2b

$$\varepsilon_b = \tfrac{1}{2}(\varepsilon_\alpha - \varepsilon_\beta) \quad (1)$$

$$\varepsilon_a = \tfrac{1}{2}(\varepsilon_\alpha + \varepsilon_\beta) \quad (2)$$

Bending strain in the vertical plane

To justify the measurement of strain only in the horizontal plane, the pipes in Test 01 were installed to measure the vertical strains developed due to strike-slip faulting. This was compared with data from Test 05, where the pipes were installed to measure horizontal pipe strains. The measured bending strains, ε_b, for Tests 01 and 05 are plotted against distance from the fault at $\delta = 1$, 2, 3, 4 and 5 cm for line α in Fig. 7. The strains measured in line β are omitted, as they were qualitatively the same as line α, but opposite in sign. The strains that developed in the vertical plane remained constant throughout testing, whereas the strains developed in the horizontal were directly affected by the magnitude of δ (Fig. 7). These data provided ample evidence to justify the lack of vertical strain measurement for the remaining tests.

Axial strain, ε_a

The strains developed in the axis of the instrumented pipe were computed as the average of the α and β strain values for gauges at the same position number on the pipe (equation (2)), with the resulting positive strains representing net tension, and negative strains representing compression. A typical plot of longitudinal axial strain ε_a over the length of the pipe is presented in Fig. 8, which shows strains as large as 50 $\mu\varepsilon$ within the central 40 cm of the pipe, and reducing to zero at either end. It is observed that there is net tension

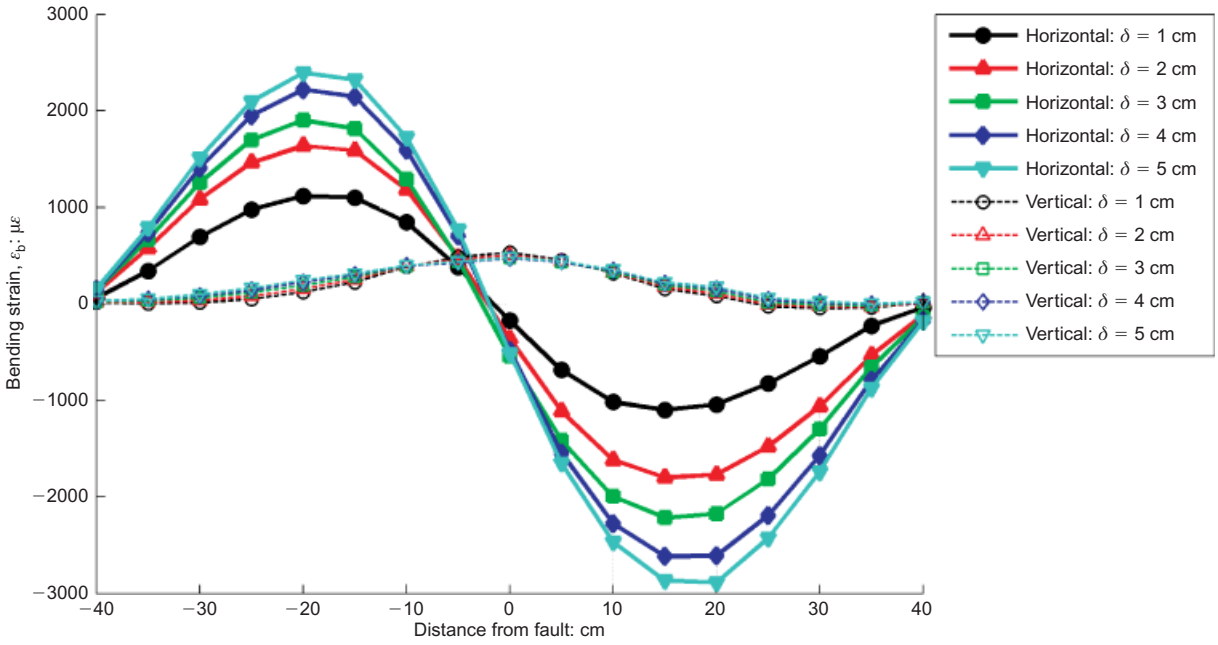

Fig. 7. Strain distribution for instrumented pipes oriented to measure horizontal and vertical strains, strain gauge line α (no shaking, $\theta = 90°$, $D_r = 60\%$, AR20, Toyoura sand)

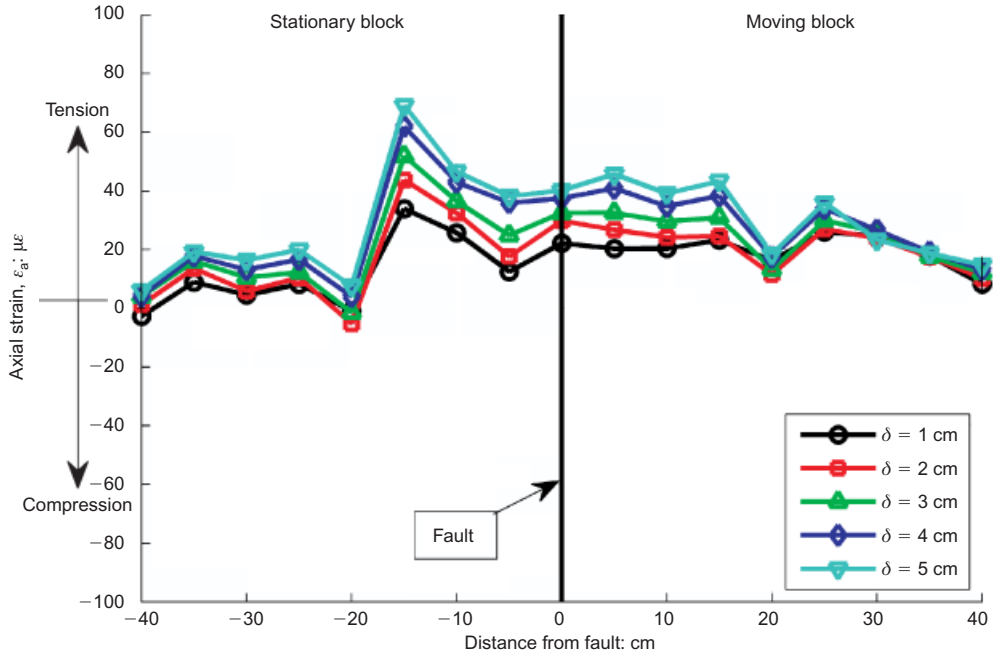

Fig. 8. Distribution of ε_a along length of the pipe, baseline case (no shaking, $\theta = 90°$, $D_r = 60\%$, AR20)

along the entire axis of the pipe when crossing a strike-slip fault at 90° (Fig. 8) resulting from the geometrical extension of the pipe due to faulting. This small magnitude of ε_a implies that the embedded model pipe has a smooth surface, and little friction develops between the pipe and the surrounding sand. Ideally, this would also be the case for a prototype pipe, because low soil–pipe friction is beneficial to pipe performance, as it reduces the potential for damage when the pipe is subjected to fault action (Kennedy *et al.*, 1977).

Bending strain, ε_b

The strains measured by the strain gauges pasted in line α along the length of the pipe at $\delta = 4$ cm for different values of θ are illustrated in Fig. 9, with the solid lines representing pipes installed to cross the fault in compression and the dotted lines representing the pipes installed to cross the fault in tension. The asymmetry of the measured strains correlated well with the surface expressions observed after testing. The recorded data indicate that only very small strains were measured by the gauges 3 cm from the ends of the pipe, as shown by Fig. 9, confirming the free-end condition of the pipe. The point of inflection of the measured strains, which represents the point of maximum shear force in the pipe, and consequently is the point where the fault plane intersects the pipe axis, is observed to vary from test to test, and can sometimes migrate by up to 10 cm as δ increases, implying that the fault development is subject to bifurcation. It is observed that the axial strains generated along the axis of the pipe (Fig. 8) are around 2% or less of the bending strains developed along the length of the pipe (Fig. 9), suggesting that faults passing through buried pipelines generate predominantly bending strains rather than axial strains. The magnitude of strain is observed to reduce with decreasing values of θ (Fig. 9), irrespective of whether the pipe is subjected to axial compression or tension during faulting. However, for smaller crossing angles in tension, the fault plane intersects the pipe further from the mid-point of the pipe on the stationary block side of the fault.

The effect of simultaneous shaking and faulting is to reduce the magnitude of bending strains, as illustrated in Fig. 10. The greatest reduction in measured strains from the no-shaking case was 77%, observed at $A_{max} = 0{\cdot}5\boldsymbol{g}$, whereas $A_{max} = 0{\cdot}8\boldsymbol{g}$ showed only a 53% reduction, and $A_{max} = 0{\cdot}2\boldsymbol{g}$ showed a 45% reduction.

The observed relationship between embedded pipe stiffness and ε_b was non-linear, with ε_b increasing rapidly for the first 25 mm of δ, as indicated by Fig. 11. Anastasopoulos & Gazetas (2010) observed similar non-linear soil–structure interaction during numerical simulations of dip-slip faulting, which were attributed to mechanism changes caused by fault bifurcation. Here the non-linear behaviour is attributed to the strain-softening soil response, as the instrumented pipe possessed a linear stress–strain relationship over the calibrated range of $\pm 5000\ \mu\varepsilon$. Additionally, the non-linear behaviour was observed at all instrumented positions along the pipe, whereas if the non-linearity had stemmed from the effects of fault bifurcation, it would be expected to occur only near the regions of shear failure within the soil.

Bifurcation of subsoil deformation during fault action generates many and complicated distribution of slip planes, both in reality (Tchalenko & Ambraseys, 1970) and in model tests (Hori *et al.*, 2002). A more complicated distribution of the bending strain development with fault displacement was observed to occur in Test 22, shown in Fig. 12. This was considered to be a result of fault bifurcation, which was observed in both the surface rupture pattern and the bending strain. In this case the bending strain distribution indicates three shear planes intersecting the pipe axis at small values of δ, as indicated by the points of inflection in Fig. 12 at $\delta = 1$ cm and 2 cm. As fault displacement progresses, the shear planes at 0 and +28 cm from the fault fade to leave a dominant failure plane at −18 cm from the fault at $\delta = 4$ cm and 5 cm. The fault bifurcation was visible in images of the soil surface after testing, with the previously level soil surface (Fig. 13(a)) displaying evidence of rupture deviating from the imposed fault line, as highlighted in Fig. 13(b). Surface ruptures were observed originating from the split of the split box, with a strike at 45° to the imposed fault line. The pipe placed at $\theta = 30°$ tension intersects the surface rupture on the stationary block, which coincides with the failure plane indicated by the recorded strains. It is perceived that this type of bifurcation-induced bending strain development is most liable to be observed in

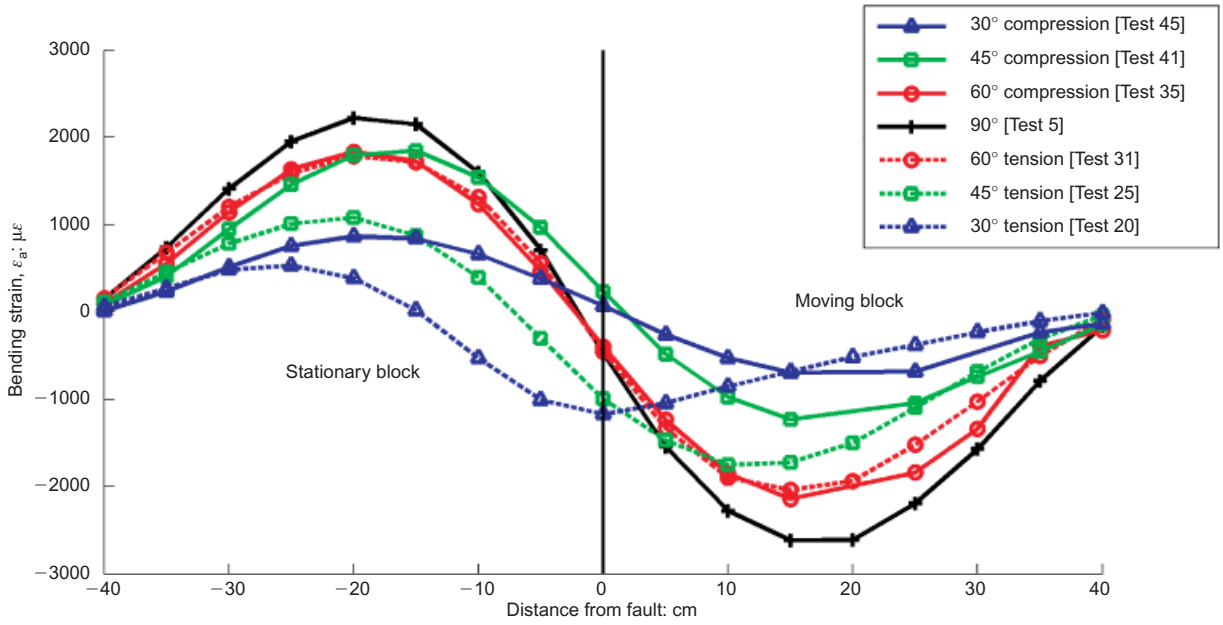

Fig. 9. Effect of pipe-fault crossing angle θ on distribution of measured strain along length of pipe at $\delta = 4$ cm (no shaking, $D_r = 60\%$, AR20)

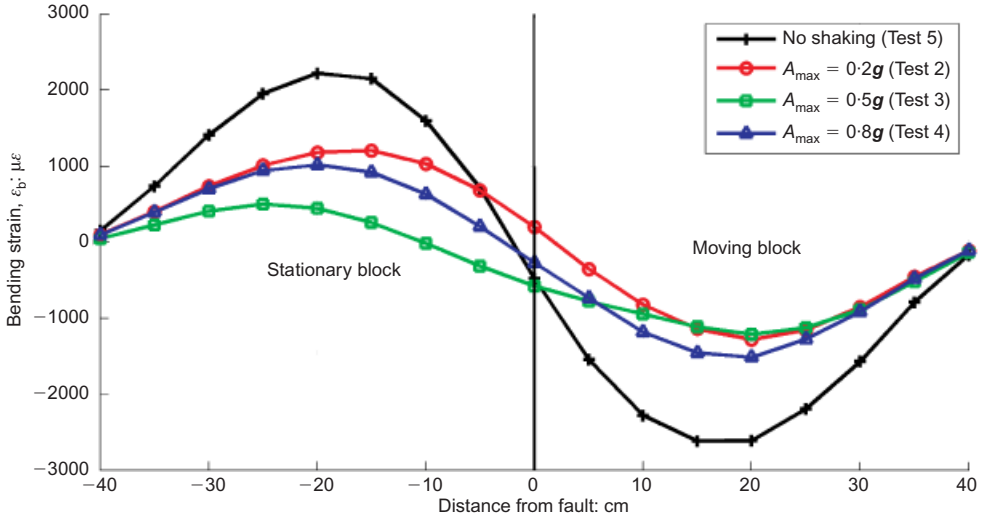

Fig. 10. Effect of pipe acceleration level A_{max} on the distribution of measured strain along length of pipe at $\delta = 4$ cm ($\theta = 90°$, $D_r = 60\%$, AR20)

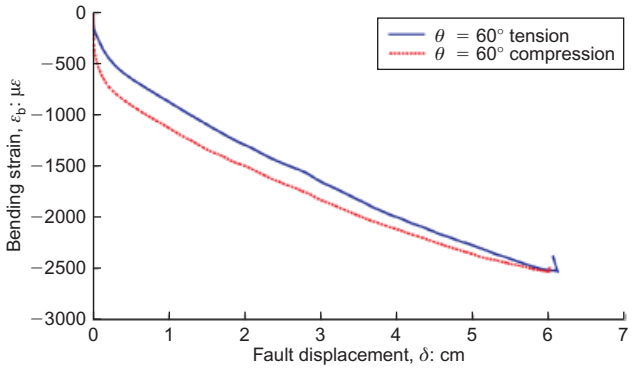

Fig. 11. Development of bending strain ε_b with fault displacement δ at 15 cm from fault on moving block (no shaking, $D_r = 60\%$, AR20)

tests performed with the pipe crossing the fault at $\theta = 30°$ tension, and was observed to some degree in all four tests performed under this condition (Tests 20–23). A pipe installed at $\theta = 30°$ tension is the only condition where the instrumented pipe is close enough to the stationary block side of side C and the moving block side of side A (Fig. 2) of the split-box apparatus to be able to intersect the surface rupture created by the split-box movement.

DISCUSSION

Level of acceleration, A_{max}

In tests where faulting and shaking were applied simultaneously there was a clear reduction in the maximum recorded bending strain ε_b compared with the static faulting case for all values of θ, as indicated by Fig. 14. However, larger values of A_{max} did not necessarily reduce the observed ε_b, with $\varepsilon_{b,max}$ exhibiting a slight increase as A_{max} increased from 0·5**g** to 0·8**g**. The observed reduction in magnitude of $\varepsilon_{b,max}$ with greater levels of acceleration (A_{max}) is believed to be a consequence of mobilisation of a fraction of the soil's strength to resist the applied cyclic deformation, reducing the capacity of the sand to generate the higher pipe–soil interaction stresses and strains observed under static faulting conditions. This effect can be viewed as being analogous to the vibro-installation of piles, where dynamic loading of soil reduces its shear strength.

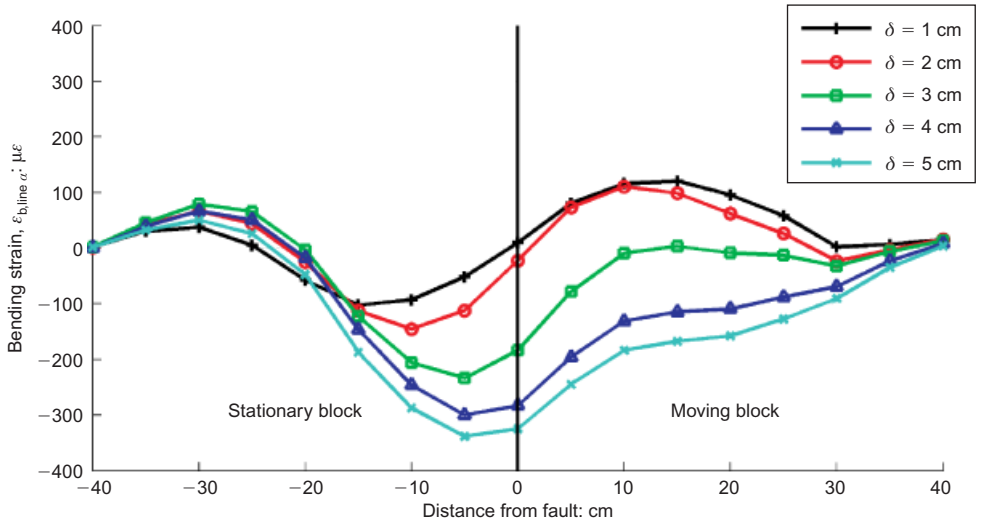

Fig. 12. Strain distribution for instrumented pipes orientated to measure horizontal and vertical strains, strain gauge line α (Test 22, $A_{max} = 0{\cdot}5g$, $\theta = 30°$ tension, $D_r = 60\%$, AR20)

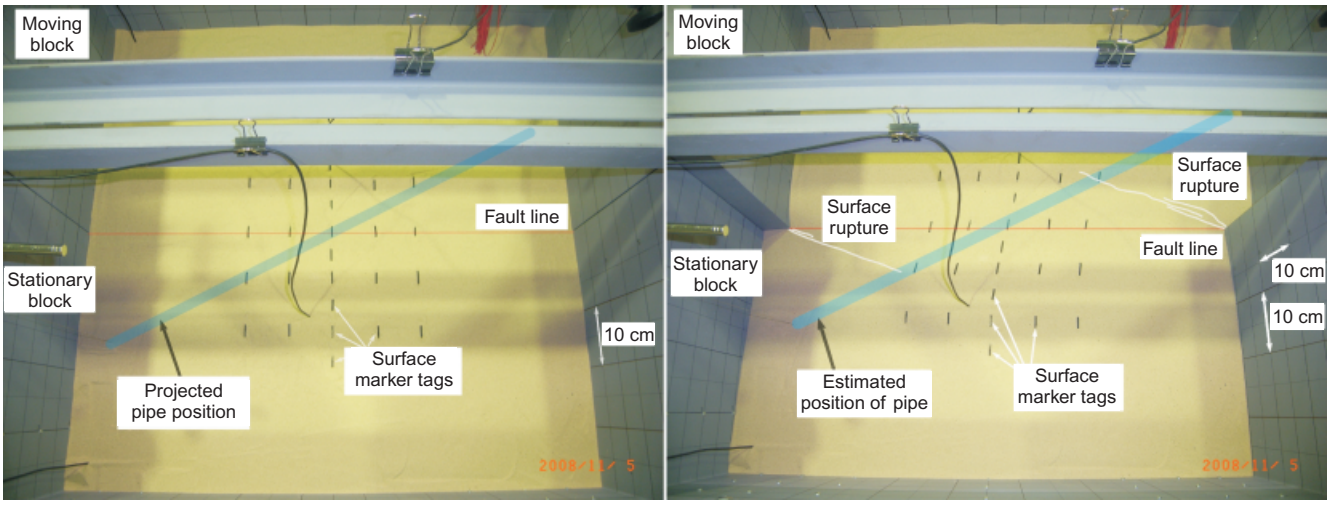

Fig. 13. Surface of Test 22 (a) before and (b) after testing ($A_{max} = 0{\cdot}5g$, $\theta = 30°$ tension, $D_r = 60\%$, AR20)

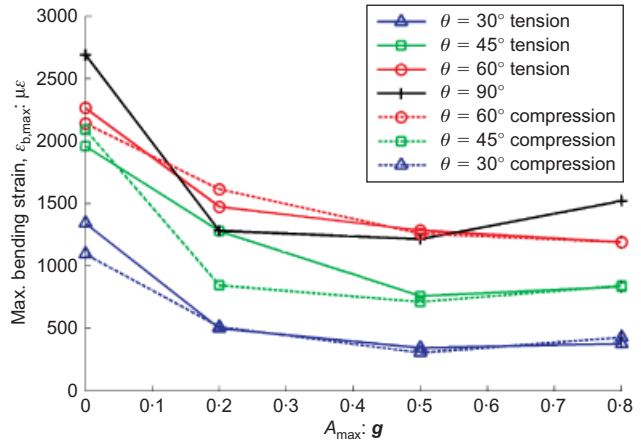

Fig. 14. Variation of maximum pipe strain with acceleration level at $\delta = 4$ cm for various pipe-fault crossing angles θ ($D_r = 60\%$, AR20)

Pipe-fault crossing angle, θ

Axial strain, ε_a. The axial strain in the pipe tended to be greatest at the central portion of the pipe, close to the imposed strike-slip fault, as shown in Fig. 8. In order to examine the effect of pipe-fault crossing angle θ on the axial strain, the maximum, minimum and mean of the axial strain over the entire length of the pipe were considered. A representative plot of the variation of these strain values when $\delta = 4$ cm for the various values of θ considered is shown in Fig. 15 (for tests performed under no shaking). It indicates that the axial strain is tensile for pipes crossing in tension (Fig. 8(a)) and compressive for pipes crossing in compression, while pipes crossing at $\theta = 90°$ tend to display net tension. Referring to Fig. 16, the net tension exhibited by pipes crossing perpendicular to the fault is deemed to be a result of the geometry of the experiment set-up; as the strike-slip fault is displaced, the pipe is subjected to elongation, resulting in axial tension.

The mean axial strain along the length of the pipe reduces

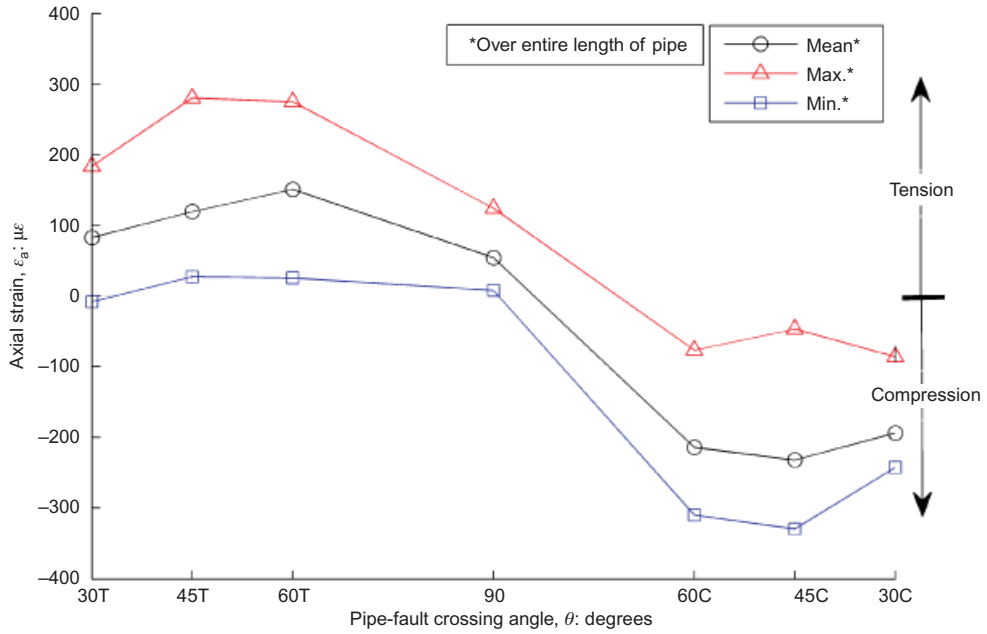

Fig. 15. Variation of mean, maximum and minimum ε_a over entire length with respect to pipe-fault crossing angle θ for no-shaking tests at $\delta = 4$ cm ($D_r = 60\%$, AR20)

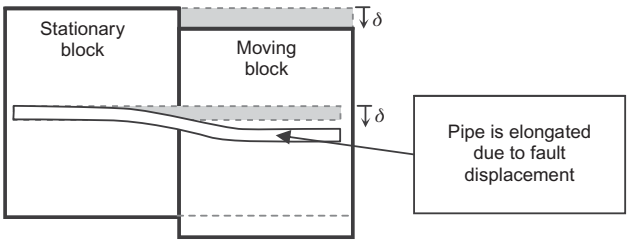

Fig. 16. Geometric effect of faulting

when faulting and shaking are applied simultaneously, as indicated by Fig. 17. The fault displacement, δ, does not affect the axial strain, suggesting that the skin friction of the pipe has been activated at the smallest level of fault displacement.

Bending strain, ε_b. The absolute value of the maximum measured strain ($|\varepsilon_{b,max}|$) along the pipe for each test was normalised relative to the test performed under the reference condition of an AR20 pipe placed at $\theta = 90°$, in sand with $D_r = 60\%$, under no shaking during faulting, at a given magnitude of fault displacement to give the strain factor, F. The strain factor for each 1 cm displacement increment was then averaged over five increments to obtain the average strain factor, $F_{av.}$. The maximum absolute strains were observed to decrease linearly with decreasing sine of the pipe-fault crossing angle for tests performed on pipes subject to the no-shaking condition, as indicated by Fig. 18. Within the range of the tested θ values, maximum absolute strains drop to 50% ± 5% of the $\theta = 90°$ (where $F_{av} = 1$) pipe value at $\theta = 30°$ (where $F_{av} = 0{\cdot}45$), for fault displacements greater than or equal to the pipe diameter. The results imply that as the pipe-fault crossing angle decreases, the lower the bending strains observed in the pipe become. This is due to smaller values of θ resulting in a larger proportion of the pipe span lying within the zone of soil deformed by the fault rupture, causing a given fault displacement to be dissipated over a greater length of pipe, and reducing the strain on the pipe.

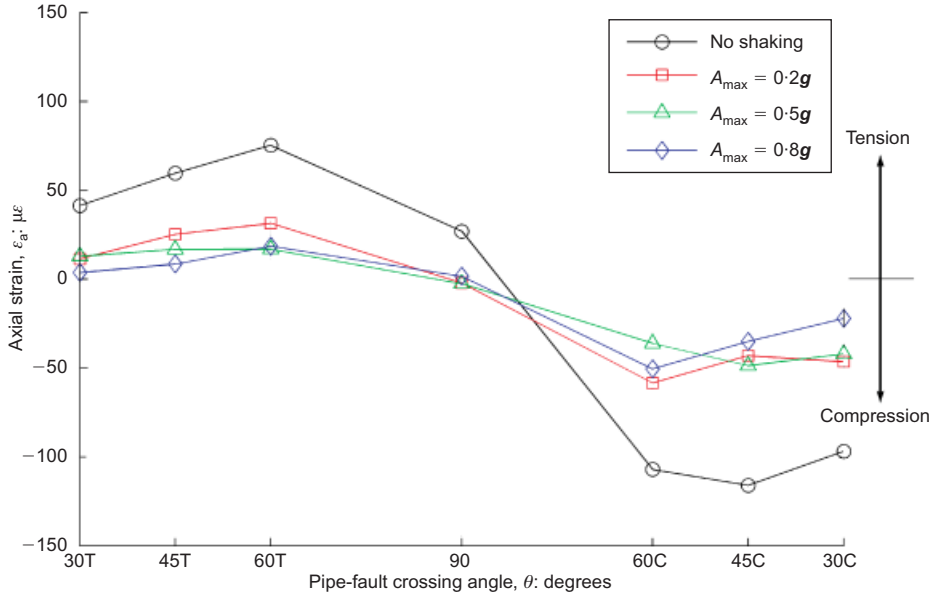

Fig. 17. Mean ε_a for tests under different levels of acceleration at $\delta = 4$ cm ($D_r = 60\%$, AR20)

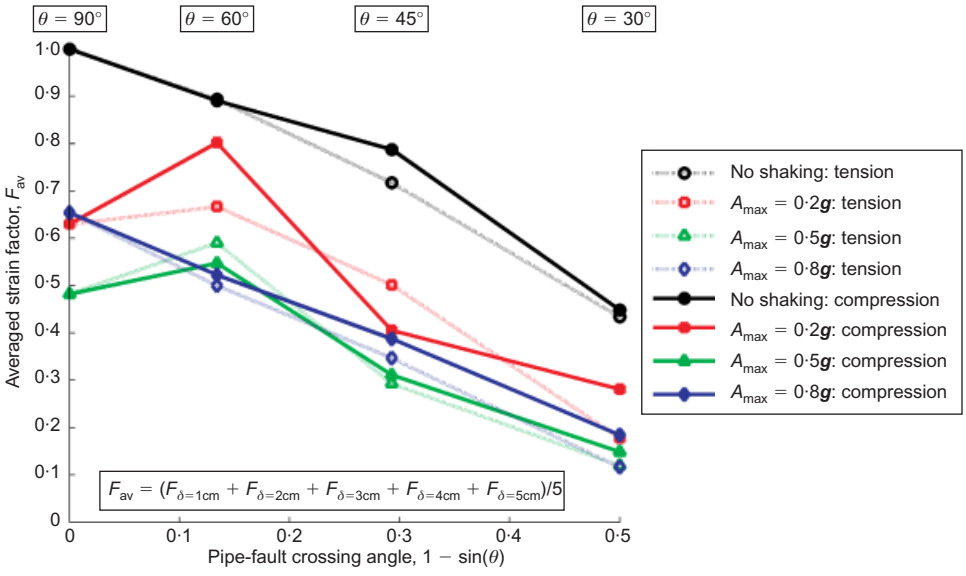

Fig. 18. Average variation of strain relative to $\theta = 90°$ over $\delta = 1$–5 cm, no shaking, at various pipe-fault crossing angles ($D_r = 60\%$, AR20)

Relative density of sand, D_r

The maxima of the absolute bending strains measured using dry Toyoura sand at relative densities of 40%, 60% and 80% were plotted against their respective relative densities to examine the influence of soil density. The influence of D_r on the absolute value of maximum bending strains ($|\varepsilon_{b,max}|$) experienced by the buried pipe at $\delta = 4$ cm, for tests subjected to no shaking and $A_{max} = 0{\cdot}5\boldsymbol{g}$, is presented in Fig. 19. Results indicate that the strains in tests where faulting and shaking were simultaneously applied are smaller than the maximum strains in tests where no shaking was applied, irrespective of the relative density of the sand (Fig. 19). Pipes faulted under static conditions exhibited a steady increase in magnitude of measured strains as D_r increased. When shaking was applied during faulting, although the magnitude of strains was reduced compared with the static case, similar magnitudes of strain were observed at $D_r = 40\%$ and 60%, and as D_r increased further to 80% there was a sharp increase in strains, reducing the difference between the no-shaking and shaking cases. This results in a reduction in the beneficial lowering of imposed strains on the buried pipe due to simultaneous faulting and shaking at higher relative densities. Whereas the increase in observed pipe strain with increasing D_r for the static, no-shaking condition is more clearly related to the associated increase in soil stiffness and therefore the increased stress on the buried pipe, the relationship between strain and soil density is a little more complex when shaking is applied. The larger reduction in strain for $D_r = 40\%$ and 60% for simultaneous faulting and shaking is attributed to the stress release due to the associated dynamic action. At the higher density of 80% the already dense soil is attempting to dilate during faulting, and the stress release due to simultaneous faulting and shaking is diminished as there are greater numbers of particle contacts for a given volume of soil.

The sharp increase in the strain response of the buried pipe to shaking at $D_r = 80\%$ draws similarities with the liquefaction resistance of soil as its density increases. Seed *et al.* (1986) showed a rapid increase in liquefaction resistance for D_r greater than 70%, and NCEER (1997) represented this key value in terms of SPT N-value, with resistance to liquefaction greatly improved as the SPT N-value increased past 22. Similarly, Andrus & Stokoe (1997) indicated a sharp increase in liquefaction resistance as shear wave velocity (V_s) exceeded 200 m/s. However, as only three relative densities were examined, this point would benefit from further study.

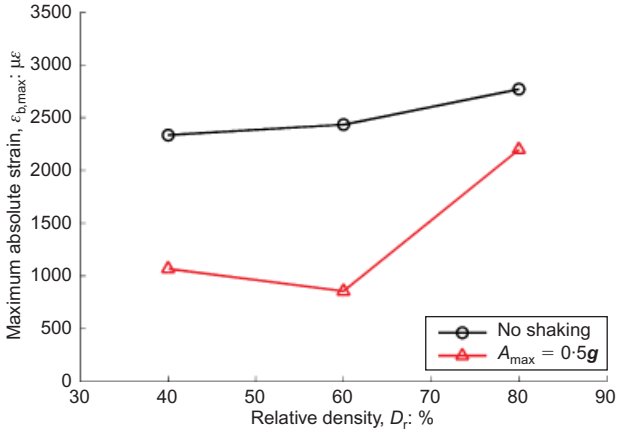

Fig. 19. Maximum strain against relative density for tests performed under no shaking and $A_{max} = 0{\cdot}5\boldsymbol{g}$ at $\delta = 4$ cm ($\theta = 90°$, AR20)

Pipe flexural rigidity, EI

The distribution of bending strain normalised by the material stiffness and second moment of inertia of the baseline pipe section (see Table 1), under no shaking and $A_{max} = 0{\cdot}5\boldsymbol{g}$, at a fault displacement of 4 cm is shown in Fig. 20. The pipes in order of increasing flexural rigidity are PE20, PE40, AR20 and AR40, as described in Table 1. The results indicate that as the flexural rigidity of the pipe increased, the maximum strains induced in the pipe decreased, as the stiffer pipes deflected less to accommodate the same pressures. Pipes with lower flexural rigidity such as PE40 and PE20, with flexural rigidities of 85% and 7% of the baseline AR20 pipe, are able to support greater concentrations of strain along the length of the pipe, whereas stiffer pipes with higher flexural rigidities, such as AR20 and

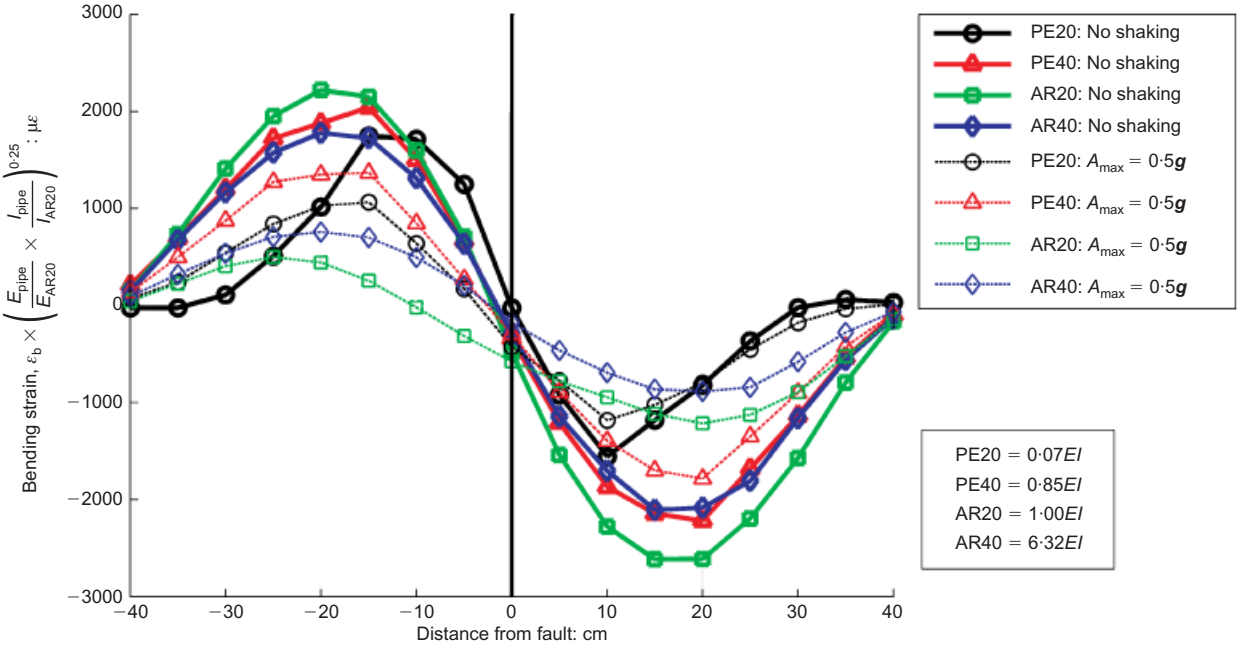

Fig. 20. Effect of pipe stiffness on strains at $\delta = 4$ cm under no shaking and $A_{max} = 0{\cdot}5\boldsymbol{g}$ ($\theta = 90°$, $D_r = 60\%$)

AR40, exhibit much more gradual changes in bending strain distribution. In contrast, the associated bending moments are much greater for pipes with higher flexural rigidity and smaller for pipes with low flexural rigidity.

Focusing on the bending strain response of PE20, with the lowest flexural rigidity of the pipes tested, the distribution of strain can be observed to be spread over a greater length of the pipe when shaking is simultaneously applied compared with tests where no shaking is applied. This suggests that applied accelerations reduce the bending strains by spreading the distribution over the length of the pipe. This is considered to be a result of the dynamic excitation altering the interparticle contact forces, allowing the pressures to be dissipated further from the shear zone of the fault plane.

By summarising the findings described above, it is reasonable to state that a pipe crossing a strike-slip fault is well protected by crossing the fault at an oblique angle (θ being less than 90°) and using a softer material in addition to, or in place of, a joint. These results are favourable when considering buried local gas pipelines subject to simultaneous faulting and synchronous shaking, as faulting stresses are distributed over a longer section of the pipe by the applied motion.

CONCLUSIONS

Shaking-table tests were performed on model pipelines, instrumented with strain gauges, under single-gravity conditions to study the effect of pipe-fault crossing angle, level of acceleration and backfill soil stiffness on the response of buried pipelines subject to right-lateral strike-slip faulting. The results demonstrate that the vertical strains generated during strike-slip faulting are less than 2% of the strains generated in the horizontal when all other testing conditions are held constant. The major conclusions drawn from this study are as follows.

(*a*) The model tests performed indicate a clear reduction in bending moment induced in pipes as the pipe-fault crossing angle θ decreases.

(*b*) The maximum absolute strains decrease linearly with $\sin\theta$ for tests performed on pipes subject to the no-shaking condition. Maximum absolute strains drop to 50% ± 5% of the $\theta = 90°$ pipe value at $\theta = 30°$, for fault displacements greater than or equal to the pipe diameter.

(*c*) Simultaneous faulting and synchronous shaking reduces the strains induced in the buried pipe, where the applied motion is uniform and sinusoidal.

(*d*) Although the fault displacement has a direct influence on the forces acting on the pipe, the cyclic induced pipe displacement is significantly smaller. It is suggested that the dynamic input from the imposed shaking acts mainly to reduce the shear strength available to resist pipe deformation, thus reducing strains and pressures incurred in the pipe.

(*e*) The greater the relative density, the larger the strains and bending moments induced in the buried pipe. It is inferred that the increase in soil stiffness associated with the increase in relative density amplifies the capacity of the soil to resist pipe deformations, and thus increases the magnitude of the pipe response. The increase in maximum bending strains is much larger for an increase in D_r from 60% to 80% than for an increase from 40% to 60%.

(*f*) Pipes made from a more flexible material result in strains being concentrated in a region closer to the fault, with larger and sharper changes in strains developed within the zone of deformation. Conversely, pipes possessing a higher *EI* are subject to more gradual changes in strain, with a smaller magnitude of strain spread over a greater length of the pipe, and strains being developed well outside the zone of deformation created by the fault.

ACKNOWLEDGEMENTS

This research would not be possible without the support provided by Tokyo Gas. The authors are also greatly indebted to the advice and expertise provided by Sugo Keiichi, Professor Junichi Koseki, Professor Muneo Hori, Associate Professor Taro Uchimura and Professor Nobuhisa Suzuki.

NOTATION

A_{max}	acceleration intensity
D_r	relative density
d_{int}	internal pipe diameter
d_{out}	outer pipe diameter
E	pipe elastic modulus
EI	pipe stiffness; pipe flexural rigidity
F	strain factor
F_{av}	average strain factor
I	pipe second moment of inertia
t	pipe thickness
V_s	shear wave velocity
δ	magnitude of fault displacement
ε_a	axial strain
ε_b	bending strain
$\varepsilon_{b,max}$	maximum value of bending strain
$\lvert\varepsilon_{b,max}\rvert$	absolute value of maximum bending strains
ε_α	strain gauge reading along line α
ε_β	strain gauge reading along line β
θ	pipe-fault crossing angle

REFERENCES

Abdoun, T. H., Ha, D., O'Rourke, M. J., Symans, D., O'Rourke, T. D., Palmer, M. C. & Stewart, H. E. (2009). Factors influencing the behavior of buried pipelines subjected to earthquake faulting. *Soil Dynam. Earthquake Engng* **29**, No. 3, 415–427.

Anastasopoulos, I. & Gazetas, G. (2010). Analysis of cut-and-cover tunnels against large tectonic deformation. *Bull. Earthquake Engng* **8**, No. 2, 283–307.

Andrus, R. D. & Stokoe, K. H. (1997). Liquefaction resistance based on shear wave velocity. In *Proceedings of the NCEER workshop on evaluation of liquefaction resistance of soils*, Technical Report NCEER-97-0022. (eds T. Y. Youd and I. M. Idriss), pp. 89–128. Buffalo, NY, USA: National Center for Earthquake Engineering Research.

Bray, J. (2001). Developing mitigation measures for the hazards associated with earthquake surface fault rupture. *Proceedings of the workshop on seismic fault-induced failure: Possible remedies for damage to urban facilities*, Tokyo, pp. 55–79.

Desmond, T. P., Power, M. S., Taylor, C. L. & Lau, R. W. (1995). Behavior of large diameter pipelines at fault crossing. *Proc. 4th US Nat. Conf. on Lifeline Earthquake Engineering, San Francisco, CA*, 296–303.

Ha, D., Abdoun, T. H., O'Rourke, M. J., Symans, M. D., O'Rourke, T. D., Palmer, M. C. & Stewart, H. E. (2008). Centrifuge modelling of earthquake effects on buried high-density polyethylene (HDPE) pipelines crossing fault zones. *J. Geotech. Geoenviron. Engng ASCE* **134**, No. 10, 1501–1515.

Hori, M., Anders, M. & Gotoh, H. (2002). Model experiment and numerical simulation of surface earthquake fault induced by lateral strike slip. *Struct. Engng Earthquake Engng JSCE* **19**, No. 2, 227–236.

Iai, S. (1989). Similitude for shaking table tests on soil-structure-fluid model in 1g gravitational field. *Soils Found.* **29**, No. 1, 105–118.

Kennedy, R. P., Chow, A. W. & William, R. A. (1977). Fault movement effects on buried oil pipeline. *J. Transp. Engng ASCE* **103**, No. 5, 617–632.

Konagai, K. (2005). Data archives of seismic fault-induced damage. *Soil Dynam. Earthquake Engng* **25**, No. 7–10, 559–570.

Koyama, Y. & Tani, K. (2003). Analysis of shear band structure

developed on surface of sand layer observed in strike-slip fault model tests. *Proc. Jap. Soc. Civ. Engrs* **750**, No. III-65, 171–181 (in Japanese).

Newmark, N. M. & Hall, W. J. (1975). Pipeline design to resist large fault displacement. *Proc. 1975 US Nat. Conf. on Earthquake Engineering, Ann Arbor, MI*, 416–425.

NCEER (1997). *Proceedings of the NCEER workshop on evaluation of liquefaction resistance of soils*, Salt Lake City, UT, Technical Report NCEER-97-0022. Buffalo, NY, USA: National Center for Earthquake Engineering Research.

O'Rourke, T. D., Jezerski, J. M., Olson, N. A., Bonneau, A. L., Palmer, M. C., Stewart, H. E., O'Rourke, M. J. & Abdoun, T. (2008). Geotechnics of pipeline system response to earthquakes. In *Geotechnical earthquake engineering and soil dynamics IV*, Geotechnical Special Publication 181 (eds D. Zeng, M. T. Manzari and D. R. Hiltunen). Reston, VA, USA: ASCE (CD-ROM).

Rathje, E. M., Kelson, K., Ashford, S. A., Kawamata, Y., Towhata, I., Kokusho, T. & Bardet, J. P. (2006). Geotechnical aspects of the 2004 Niigata Ken Chuetsu, Japan, earthquake. *Earthquake Spectra* **22**, No. S1, S23–S46.

Seed, H., Wong, R., Idriss, I. & Tokimatsu, K. (1986). Moduli and damping factors for dynamic analysis. *J. Geotech. Engng ASCE* **112**, No. 11, 1016–1032.

Takada, S., Hassani, N. & Fukuda, K. (2001). Propose of simplified method for buried pipes crossing earthquake fault. *Proc. Jap. Soc. Civ. Engrs* **668**, No. I-54, 187–194 (in Japanese).

Taniyama, H. & Watanabe, H. (1998). Deformation of sandy deposit by reverse faulting. *Proc. Jap. Soc. Civ. Engrs* **591**, No. I-43, 313–325 (in Japanese).

Tchalenko, J. S. & Ambraseys, N. N. (1970). Structural analysis of the Dasht-e-Bayaz (Iran) earthquake fractures. *Bull. Geol. Soc. Am.* **81**, No. 1, 41–60.

Trautmann, C. H. & O'Rourke, T. D. (1985). Lateral force-displacement response of buried pipe. *J. Geotech. Engng ASCE* **111**, No. 9, 1077–1092.

Towhata, I. (2008). *Geotechnical earthquake engineering*, p. 13. Berlin, Germany: Springer.

Ueta, K. & Tani, K. (1999). *Deformation of Quaternary deposits and ground surface caused by bedrock fault movements. Part 2: Normal and reverse fault model tests*, Report No. U98048. Chiba: CRIEPI (Central Research Institute of Electric Power Industry) Abiko Research Laboratory.

Wang, L. L. R. & Wang, L. J. (1995). Parametric study of buried pipelines due to large fault movement. *Proc. 4th US Nat. Conf. on Lifeline Earthquake Engineering, San Francisco, CA*, 152–159.

Wang, L. R. L. & Yeh, Y. H. (1985). A refined seismic analysis and design of buried pipeline for fault movement. *Earthquake Engng Struct. Dynam.* **13**, No. 1, 75–96.

Yasuda, S. & Hori, M. (2006). Framework of design procedures of pipeline structures against surface earthquake faulting. *Proc. 2nd Japan-Taiwan Joint Workshop, Japanese Geotechnical Society and Taiwan Geotechnical Society, Nagaoka*, 232–235.

Yasuda, S., Numata, D. & Mayuzumi, S. (2007). Model tests on the influence of surface fault rupture on the damage of pipes, houses and embankments. *Proc. 2nd Int. Geotechnical Symp. on Geotechnical Engineering for Disaster Prevention and Reduction, Yuzhno-Sakhalinsk*, 531–537.